



Spontaneous regeneration of active sites against catalyst deactivation

Kai Feng^{a,d,1}, Jiajun Zhang^{b,1}, Zhengwen Li^a, Xiaozhi Liu^c, Yue Pan^c, Zhiyi Wu^d,
Jiaming Tian^a, Yuxin Chen^a, Chengcheng Zhang^d, Qiangqiang Xue^a, Le He^d, Xiaohong Zhang^d,
Yujun Wang^a, Bin Yang^b, Dong Su^c, Kai Hong Luo^{b,e,*}, Binhang Yan^{a,**}

^a Department of Chemical Engineering, Tsinghua University, Beijing 100084, China

^b Center for Combustion Energy, Key Laboratory for Thermal Science and Power Engineering of Ministry of Education, International Joint Laboratory on Low Carbon Clean Energy Innovation, Tsinghua University, Beijing 100084, China

^c Beijing National Laboratory for Condensed Matter Physics, Institute of Physics, Chinese Academy of Sciences, Beijing 100084, China

^d Institute of Functional Nano & Soft Materials (FUNSOM), Jiangsu Key Laboratory of Advanced Negative Carbon Technologies, Soochow University, Suzhou 215123, China

^e Department of Mechanical Engineering, University College London, London WC1E 7JE, UK

ARTICLE INFO

Keywords:

Dry reforming of methane
Catalyst deactivation
Structural sensitivity
Local redox environment
Spontaneous regeneration

ABSTRACT

Catalyst deactivation is one of the long-standing challenges in heterogeneous catalysis. Here, we found that the Ni/MgAl₂O₄ catalyst shows an atmosphere-dependent deactivation behavior during dry reforming of methane (DRM) process, i.e., oxidation and redispersion of Ni near the inlet in an oxidizing atmosphere while coking and sintering of Ni near the outlet in a reducing atmosphere. These structural evolutions of the Ni species are revealed to be driven by the surface oxidation degree of the catalyst, such that it is reversible when the redox atmosphere changes. It inspired us to develop an alternating-feeding gas strategy that periodically changes the gas flow direction to balance the structural evolution of Ni species across catalyst bed through the spontaneous regeneration of deactivated sites, enabling a supra-stable DRM process. This study provides new insights into the catalyst deactivation for DRM process, while opens a new avenue to address catalyst deactivation in various redox-catalyzed processes.

1. Introduction

Catalyst deactivation is a long-standing challenge in heterogeneous catalysis, which generally requires plant shutdown to replace or regenerate deactivated catalysts at significant capital costs [1–4]. Over the past century, the main deactivation pathways have been identified as sintering [5–7], poisoning [8–10], or decomposition [11–13] of active sites under harsh operating conditions. Therefore, researchers have proposed various strategies based on catalyst design or reaction engineering to enhance heterogeneous catalytic stability. A typical example is the fluid catalytic cracking process that enables *in-situ* regeneration of deactivated catalysts, however, it still requires additional regeneration units leading to increased industrial costs [14–16]. Moreover, clever nanostructure design or electronic structure engineering for catalysts can also contribute to enhanced catalytic stability but usually at the

expense of some loss of activity [17–20]. Optimizing metal-support interaction (MSI) remains the best choice for industrial catalyst design to improve structural stability and a volcano-like relationship has been revealed based on kinetic simulations for a large number of metal-support pairs model [21,22]. However, the thermal stability of active sites is not only related to MSI but also sensitive to the local redox environment [23–26]. It has been found that active palladium (Pd) atoms could reversibly move into and out of the perovskite lattice in cycles between oxidative and reductive environments while such “intelligent” property is also considered responsible for excellent catalytic stability exhibited by Pd-perovskite catalysts [27]. For most catalytic reactions, changes in the redox environment occur as reactions proceed thus inevitably affecting the structural stability of active sites [28,29]. The understanding and optimization of the structural sensitivity of catalysts to the redox environment of a specific catalytic process

* Corresponding author at: Center for Combustion Energy, Key Laboratory for Thermal Science and Power Engineering of Ministry of Education, International Joint Laboratory on Low Carbon Clean Energy Innovation, Tsinghua University, Beijing 100084, China.

** Corresponding author.

E-mail addresses: k.luo@ucl.ac.uk (K.H. Luo), binhangyan@tsinghua.edu.cn (B. Yan).

¹ These authors contributed equally to this work.

may provide an attractive strategy for mitigating catalyst deactivation.

Herein, the dry reforming of methane (DRM) reaction, a promising catalytic process for large-scale carbon fixation and high-volume chemicals production but suffering from catalyst deactivation [30–33], was employed as a model reaction to investigate the structural sensitivity of active sites to the local redox environment in high-temperature heterogeneous catalysis. As a typical catalytic process involving redox cycling, the catalytic stability of DRM catalysts is inevitably affected by its structural sensitivity to the redox atmosphere under reaction conditions. It has been widely reported that oxidation, sintering, and coking of active sites in DRM catalysts during reaction can directly lead to catalyst deactivation, which is generally attributed to inconsistent dissociation rates of methane and carbon dioxide on these catalysts [12,13]. Additionally, due to high feedstock conversion during the DRM process, there exists a non-uniform distribution of the local redox environment along the catalyst bed, which results in different causes for catalyst deactivation. In this work, we demonstrated that the deactivation of Ni/MgAl₂O₄ catalysts is location-dependent/atmosphere-dependent, i.e., oxidation and redispersion of Ni particles near the inlet in a slightly oxidizing atmosphere while coking and sintering of Ni particles near the outlet in a highly reducing atmosphere. The redispersion and the sintering of Ni particles were successfully monitored and confirmed to be reversible when the redox atmosphere changes. This inspires us to propose an inlet-outlet switching strategy that periodically changes the gas flow direction to enable spontaneous regeneration of active sites, achieving a supra-stable DRM process using industrially viable Ni/MgAl₂O₄ catalysts.

2. Experimental

2.1. Catalyst preparation

MgAl₂O₄ support was synthesized through a co-precipitation method using a two-stage membrane dispersion microreactor as previously reported [34]. Supported catalysts were synthesized through an impregnation method. Typically, 1 g support (MgAl₂O₄, SiO₂, ZrO₂) was mixed with an aqueous solution of Ni(NO₃)₂·6 H₂O and then the water was evaporated at 80 °C under stirring to form a slurry. The feeding amount of Ni(NO₃)₂·6 H₂O was calculated based on a Ni loading of 4 wt%. After being dried at 100 °C overnight, the powder products were calcined at 400 °C in air for 4 h in a muffle furnace.

2.2. Structural characterization

Transmission electron microscope (TEM) and energy dispersive X-ray spectroscopy (EDX) elements mapping images were obtained with a FEI Talos F200X TEM operating at 200 kV. *In-situ* TEM images were obtained with a Titan Themis G3 ETEM operating at 300 kV with an *in-situ* vapor thermal holder (Climate, Dens solution). X-ray diffraction (XRD) data were collected at the BL14B1 beamline of the Shanghai Synchrotron Radiation Facility (SSRF) using a 0.06887 nm wavelength X-ray. Ultraviolet-visible (Uv-vis) diffuse reflectance spectra were obtained with a Lambda 950 UV/visible/near-infrared spectrometer from PerkinElmer and an integrating sphere with a diameter of 150 mm. X-ray absorption spectroscopy (XAS) experiments were performed at the 4B9A and 1W1B beamlines of the Beijing Synchrotron Radiation Facility (BSRF).

2.3. Temperature-programmed experiments

H₂ temperature-programmed reduction (H₂-TPR) of catalysts was performed in a flow reactor. 20 mg catalyst was loaded into a quartz tube and the reactor was heated up to 400 °C in an Ar flow (20 ml/min) for 30 min for dehydration and degassing. Next, after cooling down to room temperature, the inlet flow was switched to a 20 ml/min 10 vol% H₂/Ar flow and the reactor was heated up to 800 °C with a heating rate

of 10 °C/min. The H₂ consumption was detected online using a thermal conductive detector (TCD, Agilent 8860).

Temperature-programmed oxidation (TPO) of catalysts was performed in a flow reactor. 5 mg spent catalyst was loaded into a quartz tube and the reactor. Next, the reactor was heated up to 800 °C with a heating rate of 10 °C/min under a 20% O₂/Ar atmosphere. The produced CO₂ was detected online using a Fourier transform infrared (FTIR) spectrometer (Thermo Nicolet iS20).

2.4. Catalytic performance evaluation

Dry reforming of methane (DRM) experiments were performed in a flow reactor under atmospheric pressure. Typically, 30 mg catalyst (40–60 mesh) was loaded into a quartz tube with an inner diameter of 4 mm and held in place by quartz wool. The height of the catalyst bed in this study is approximately 40 mm and the catalyst is placed vertically. Then, the reactor was heated to 800 °C with a heating rate of 10 °C/min under an N₂ atmosphere. Next, a 80 ml/min (CO₂:H₂:N₂ = 1:1:2) CH₄/CO₂/N₂ flow was switched to the reactor to perform the reaction, while the catalyst is in an N₂-protected atmosphere during the post-reaction cooling process. The regeneration process is to switch off the CH₄ gas feeding during the DRM catalytic process for 1 h.

The products were online detected using a gas chromatograph (Agilent 7890B) equipped with a flammable ionization detector (FID) and a TCD. The conversions of CO₂ (X_{CO_2}) and CH₄ (X_{CH_4}) are defined as:

$$X_{\text{CO}_2} = \frac{F_{\text{CO}_2(\text{inlet})} - F_{\text{CO}_2(\text{outlet})}}{F_{\text{CO}_2(\text{inlet})}} = \frac{\frac{C_{\text{CO}_2(\text{inlet})}}{C_{\text{N}_2(\text{inlet})}} - \frac{C_{\text{CO}_2(\text{outlet})}}{C_{\text{N}_2(\text{outlet})}}}{\frac{C_{\text{CO}_2(\text{inlet})}}{C_{\text{N}_2(\text{inlet})}}} \quad (1)$$

$$X_{\text{CH}_4} = \frac{F_{\text{CH}_4(\text{inlet})} - F_{\text{CH}_4(\text{outlet})}}{F_{\text{CH}_4(\text{inlet})}} = \frac{\frac{C_{\text{CH}_4(\text{inlet})}}{C_{\text{N}_2(\text{inlet})}} - \frac{C_{\text{CH}_4(\text{outlet})}}{C_{\text{N}_2(\text{outlet})}}}{\frac{C_{\text{CH}_4(\text{inlet})}}{C_{\text{N}_2(\text{inlet})}}} \quad (2)$$

where F is the flow rate of reactants or products (mol/min), C is the concentration of reactants or products (%).

The deactivation rate constant (k_d) is defined as:

$$k_d = \frac{\ln\left(\frac{1-X_{\text{Final}}}{X_{\text{Final}}}\right) - \ln\left(\frac{1-X_{\text{Initial}}}{X_{\text{Initial}}}\right)}{t} \quad (3)$$

where X_{Final} is the conversion after deactivation, X_{Initial} is the initial conversion, t is the reaction time.

2.5. Computational methods

The first-principle density functional theory plus dispersion (DFT-D) calculations were implemented in the Vienna Ab-initio Simulation Package (VASP) with dispersion corrections by the D3 method of Grimme. The generalized gradient corrected approximation (GGA) treated by the Perdew-Burke-Ernzerhof (PBE) exchange-correlation potential was used to calculate the exchange-correlation energy [35, 36]. The PAW pseudopotential was employed as the scheme in the representation of reciprocal space for all the elements [37,38]. The plane-wave cut-off energy was set to 520 eV for all the calculations. The Brillouin zone was sampled using a $2 \times 2 \times 1$ and $5 \times 5 \times 1$ Monkhorst-Pack k-point for respective geometry optimization and static electron structures calculation. Spin polarization has been considered, and the self-consistent field (SCF) tolerance was set to 10^{-4} eV/atom. All the modelling was performed with a convergence threshold of 0.03 eV/Å on maximum force. No symmetry constraint was used for any modelling. The computational method is believed to give high precision results, evidenced by the validation of lattice constant for the spinel lattice (primitive cell) in this study; the difference between the computational value (8.13 Å) and the reported experimental value (8.08 Å) is acceptable, as shown in Fig. S1a [39].

Slab models of Ni₁-doped MgAl₂O₄ and NiO were adopted to evaluate the oxygen removal energy, as shown in Fig. S2, and in this study the energy (E_r) was determined by the difference between the energies of the product and the reactant, as shown in Eq. 1, where E_{cat} and $E_{cat,vac}$ are the total energies of the intact catalyst and the catalyst with one oxygen vacancy respectively, and E_{H_2O} and E_{H_2} are the energies for H₂ and H₂O molecules.

$$E_r = E_{cat,vac} + E_{H_2O} - (E_{cat} + E_{H_2}) \quad (4)$$

The models for the investigation of structure evolution of the catalysts were based on a three-layer P (3 × 3) super-cell of MgAl₂O₄ spinel (1 1 1) facet, as shown in Fig. S1b. The top two layers were relaxed during calculation while the bottom layers were fixed. A 15 Å vacuum

region was created above the top layer of the graphite facet. The oxygen richness of each facet was considered by tuning different cap layers of the nature facet. MedeA 3.1.0 was used for model establishment and pseudopotential assembling for the calculation. Geometry optimization was implemented to obtain the initial state of each structure. AIMD was carried out based on the NVT ensemble at 1074 K to resemble the real experimental conditions, with a step size of 2 fs. Bader charge was calculated for atomic electron analysis.

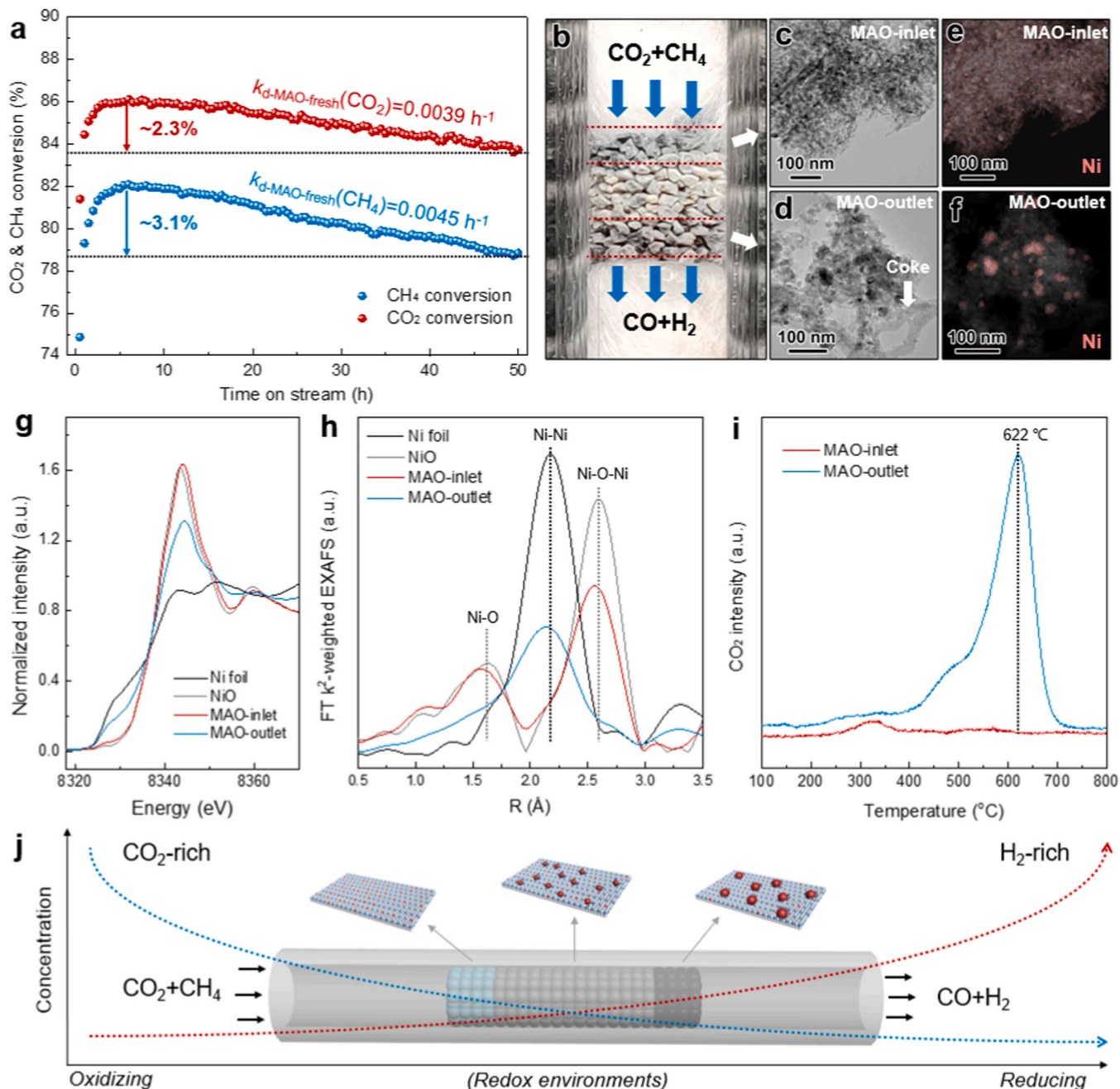


Fig. 1. (a) Evolution of CH₄ and CO₂ conversion for Ni/MgAl₂O₄ during 50-h DRM catalytic reaction at 800 °C (30 mg catalysts, 40–60 mesh, CO₂/CH₄/N₂ = 20/20/40 ml/min). (b) Digital photo of Ni/MgAl₂O₄ after 50-h DRM catalytic reaction. (c), (d) TEM and (e) (f) EDX elemental mapping images, (g) XANES and (h) EXAFS spectra, and (i) TPO curves for MAO-inlet and MAO-outlet. (j) Schematic illustration for the structural sensitivity of Ni nanoparticles on MgAl₂O₄ to redox environment during DRM reaction.

3. Results and discussion

3.1. Local redox environment induced by DRM

The DRM reaction is a typical redox catalytic process, in which the catalyst surface would be oxidized by CO_2 dissociation while being reduced by CH_4 activation, leading to the development of the chemical looping CH_4 - CO_2 reforming process for syngas production [40,41]. In the conventional DRM process, the catalyst is exposed to a H_2 -rich reducing atmosphere due to the high conversion of CO_2 and CH_4 , in which the sintering of Ni particles is accelerated. We have previously revealed that Ni-doped MgAl_2O_4 with highly dispersed Ni and strong interaction between Ni and MgAl_2O_4 shows superior structural stability in a reducing environment [42]. Smaller Ni particles and stronger metal-support interaction are expected to provide more active sites to obtain higher activity and exhibit better anti-sintering ability to achieve better stability [43–45]. Therefore, Ni/ MgAl_2O_4 catalysts were prepared via an industrially scalable impregnation method and packed into a fixed bed reactor without H_2 reduction treatment for DRM reaction under given reaction conditions ($\text{CO}_2/\text{CH}_4/\text{N}_2$ ratio of 1/1/2, 160,000 $\text{ml}\cdot\text{g}_{\text{cat}}^{-1}\cdot\text{h}^{-1}$, 0.1 MPa, 800 °C). As shown in Fig. 1a and S3, the as-prepared Ni/ MgAl_2O_4 catalyst shows an activation period of ~ 5 h due to the reduction of NiO before achieving a CH_4 conversion of $\sim 82\%$ and CO_2 conversion of $\sim 86\%$ with a H_2/CO ratio of ~ 0.92 . The space-time yield (STY) is identified as 1.97 and 1.81 $\text{mol}\cdot\text{g}_{\text{cat}}^{-1}\cdot\text{h}^{-1}$ for CO and H_2 , respectively. Such catalytic activity has an advantage over conventional oxide-supported Ni catalysts (Fig. S4 and Table S1). However, as the reaction proceeds, CH_4 and CO_2 conversions start to decrease and show a decrease of $\sim 2.3\%$ (deactivation rate constant $k_d = 0.0039 \text{ h}^{-1}$) and $\sim 3.1\%$ ($k_d = 0.0045 \text{ h}^{-1}$) after 50-h catalytic reaction, respectively, which is unacceptable for large-scale DRM industrial applications. It is necessary to understand the origin of catalyst deactivation to further enhance the stability.

After 50-h DRM reaction, the catalyst bed changes from homogeneous gray (Fig. S5) to a color variation from light green to black along with the gas feeding direction (Fig. 1b). To understand this phenomenon, the catalysts near the inlet (MAO-inlet) and outlet (MAO-outlet) were collected for various characterization. As shown in Fig. 1c and d, the TEM image reveals no obvious Ni nanoparticles on MgAl_2O_4 support for MAO-inlet, while the EDX elemental mapping image shows a homogeneous distribution of Ni species in MAO-inlet, implying that Ni might be redispersed into the support to form $\text{MgNiAl}_2\text{O}_x$ or NiO- MgO solid solution [12,46]. In contrast, it is found that there are obvious Ni nanoparticles and a small amount of coke distributed on MgAl_2O_4 support for MAO-outlet, suggesting that sintering of active Ni species and coking lead to deactivation (Fig. 1e, f, and S6). That is, the redispersion of Ni species into MgAl_2O_4 support near the inlet as well as the sintering of Ni and coking near the outlet jointly contribute to the loss of active sites, which rarely occurs simultaneously. The location-dependent deactivation behaviors are further demonstrated by X-ray near edge absorption structure (XANES) spectra, extend X-ray absorption fine structure (EXAFS) spectra, and temperature-programmed oxidation (TPO) results. As shown in Figs. 1g, h, and S7, Ni in MAO-inlet shows an oxidation state similar to that of NiO standard sample but with shorter Ni-O bond length, corresponding to the redispersion of Ni species into MgAl_2O_4 support [47,48]. While Ni in MAO-outlet exhibits a lower valence state than that in MAO-inlet and the coordination structure is dominated by metallic Ni-Ni bonding, implying the presence of more metallic Ni. Moreover, a significant CO_2 peak observed in the TPO experiment (Fig. 1i) indicates the generation of coke on MAO-outlet. Therefore, we can infer that the oxidation and redispersion of Ni species into MgAl_2O_4 near the inlet and the sintering of Ni species and coking near the outlet are responsible for catalyst deactivation in DRM over Ni/ MgAl_2O_4 . This location-dependent deactivation behavior may be attributed to differences in the local redox atmosphere resulting from high feedstock conversion. A similar behavior was also observed for the

pre-reduced catalyst (Fig. S8). As shown in Fig. 1j, Ni species near the inlet are exposed to a CO_2 -rich and CH_4 -rich atmosphere as the conversion is low, while Ni species near the outlet will be exposed to a CO-rich and H_2 -rich atmosphere. For Ni/ MgAl_2O_4 catalysts, the former atmosphere is slightly oxidizing and leads to the redispersion of Ni species, while the latter atmosphere is highly reducing and results in the sintering of Ni species and coking. That is, the catalytic stability of Ni/ MgAl_2O_4 is determined by its structural stability in various redox environments.

3.2. Structural sensitivity to redox environment

The structural sensitivity of the Ni/ MgAl_2O_4 catalyst to a redox environment was systematically investigated, in which the as-prepared Ni/ MgAl_2O_4 catalysts were successively subjected to oxidizing and reducing atmospheres to study the structural evolution of Ni (Fig. 2a). Firstly, the *in-situ* TEM characterization was directly employed to confirm the structural evolution of Ni on MgAl_2O_4 support in different redox environments. As shown in Fig. 2b, it is found that NiO nanoparticles are uniformly dispersed on MgAl_2O_4 support for the as-prepared Ni/ MgAl_2O_4 catalyst under an oxidizing atmosphere at 200 °C but disappear when elevating the temperature to 800 °C (Fig. 2c). The disappeared nanoparticles (~ 14.2 nm) reappear as metallic Ni particles with a smaller particle size (~ 6.7 nm) on MgAl_2O_4 when exposed to a reducing atmosphere at 800 °C (Figs. 2d and S9). This demonstrates that Ni species on MgAl_2O_4 could be redispersed into the support under an oxidizing atmosphere, while sintered under a strongly reducing atmosphere. The sintering of Ni nanoparticles at high temperatures is believed to be due to their high surface energy, while the redispersion of Ni under an oxidizing atmosphere strongly depends on the unique metal-support interaction, e.g., Ni nanoparticles do not redisperse but continue to grow on SiO_2 and ZrO_2 (Fig. S10). To understand the origin of the redispersion of Ni nanoparticles on MgAl_2O_4 support, Raman spectra of as-prepared Ni/ MgAl_2O_4 before and after being exposed to an oxidizing atmosphere (MAO-fresh and MAO-oxidizing) were collected. As shown in Fig. 2e, MAO-fresh shows typical NiO characteristic Raman peaks at 402 and 567 cm^{-1} , while only the spinel phase ($\text{MgNiAl}_2\text{O}_x$) characteristic Raman peaks at 408, 676, and 764 cm^{-1} are observed on MAO-oxidizing. Furthermore, a new peak at ~ 640 nm assigned to the absorption of $\text{MgNiAl}_2\text{O}_4$ in the ultraviolet-visible (UV-vis) diffuse reflectance spectrum of MAO-oxidizing is observed [49], which is associated with a color change from light gray to light green (Fig. S11). These results indicate that NiO could undergo a phase transition to the spinel phase ($\text{MgNiAl}_2\text{O}_x$) under an oxidizing atmosphere, which might be the cause of the disappearance of Ni nanoparticles.

Furthermore, as shown in Fig. 2f, the XANES spectrum of redispersed Ni species on MAO-oxidizing shows an absorption edge of Ni K-edge similar to MAO-fresh and NiO but a whiteline characteristic peak similar to that of NiAl_2O_4 . This implies that Ni in MAO-oxidizing undergoes a clear phase transition from NiO to the spinel phase ($\text{MgNiAl}_2\text{O}_x$). EXAFS spectra also indicate that the first-shell peak assigned to Ni-O bonding for MAO-oxidizing shifts toward a smaller R-value, implying a reduced Ni-O bond length. According to the fitting results of EXAFS spectra, the MAO-oxidizing shows a Ni-O bond length of 2.04 Å, which is slightly lower than that of NiO (2.10 Å, Fig. S12 and Table S2). The shortened Ni-O bond length due to the redispersion suggests an enhanced binding of Ni to coordinated O, which will strengthen the electronic-structure stability of Ni species under a reducing atmosphere. This inference is also demonstrated by the H_2 -TPR results, in which MAO-oxidizing (760 °C) shows a higher reduced peak than MAO-fresh (492 °C) (Fig. 2h). Moreover, a Ni-doped MgAl_2O_4 model was also built to quantify the energy required for the removal of coordinated O by H_2 using a DFT calculation method (Fig. S2). As shown in Fig. 2i, it is found that the H_2 -assisted removal energy of the first coordinated O is similar for both NiO and Ni_1 -doped MgAl_2O_4 , but Ni_1 -doped MgAl_2O_4 requires

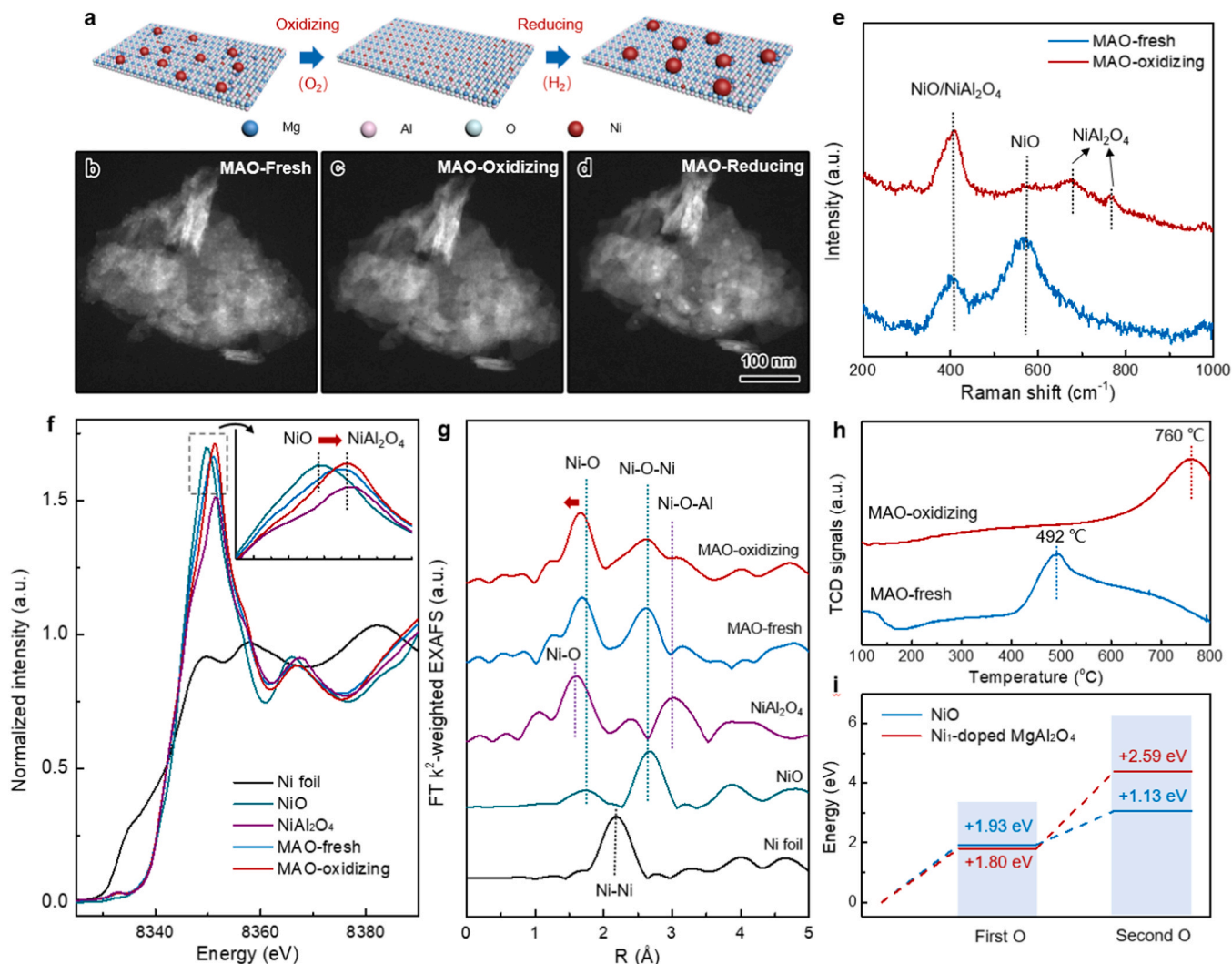


Fig. 2. (a) Schematic illustration of *in-situ* TEM experiments for structural sensitivity of Ni nanoparticles on MgAl₂O₄ spinel to redox environment. (b) *In-situ* TEM images of Ni/MgAl₂O₄ under an oxidizing atmosphere (20% O₂/Ar) at (b) 200 °C and (c) 800 °C, and (d) under a reducing atmosphere (H₂) at 800 °C. (e) Raman spectra, (f) XANES spectra, (g) EXAFS spectra, and (h) H₂-TPR curves of MAO-fresh and MAO-oxidizing. (i) H₂-assisted O removal energy of NiO and Ni₁-doped MgAl₂O₄.

more energy than NiO when the second coordinated O is further removed. Notably, such an enhanced Ni electronic structure stability makes it difficult for redispersed Ni species to be segregated and reduced to metallic Ni once the spinel phase (MgNiAl₂O₄) is formed [44]. Therefore, such a structural sensitivity of the Ni/MgAl₂O₄ catalyst to a redox environment determines its structure would be damaged under an over-oxidizing or over-reducing atmosphere and results in catalyst deactivation.

The molecular dynamics (MD) simulation was also used to further understand the structure sensitivity of Ni species to a redox environment. As shown in Fig. 3a and S13, four Ni clusters, each consisting of 6 Ni atoms, were placed on the MgAl₂O₄(111) surface to simulate a reducing atmosphere and denoted as MD-Ni, while a NiO cluster was placed on the MgAl₂O₄(111) surface with different O coverages to simulate different redox environments and denoted as MD-NiO, MD-NiO+O, and MD-NiO+OO, respectively. After 15 ps of MD calculations at 800 °C, the dispersion behaviors of Ni atoms in the four models show differences (Fig. 3b and S14). For MD-Ni and MD-NiO, the Ni atoms merge into an entire Ni cluster without showing a tendency to disperse. In contrast, for MD-NiO+O and MD-NiO+OO, the number of coordination O atoms to Ni increases, while the bonding of Ni-O-Mg and Ni-O-Al starts to appear, which is considered to be the driving force for Ni

redispersion. That is, Ni atoms tend to sinter and grow in the O-deficient model while redisperse in the O-rich models, which is consistent with the experimental results. To quantify this observation, the evolution of the distance between two neighboring Ni atoms with time (Ni12 and Ni7 for MD-Ni, Ni12 and Ni2 for MD-NiO, MD-NiO+O, and MD-NiO+OO) was further monitored. As shown in Fig. 3c, all models continuously show a similar distance of approximately 2.5 Å between the two neighboring Ni atoms, which agrees well with the typical Ni-Ni bond length in metallic Ni structure. Meanwhile, MD-NiO+O and MD-NiO+OO show an increased distance during the initial 2 ps and then keep a constant distance of around 5 Å and 7.5 Å, respectively. Additionally, the number of Ni atoms with a distance of more than 3 Å (bond length for Ni-O-Ni in NiO crystalline) from the adjacent Ni atoms was counted, and only MD-NiO+O and MD-NiO+OO have such Ni atoms (3 and 7 respectively, Fig. 3d). These results directly indicate that an increased number of O atoms could significantly promote the redispersion of Ni atoms. This conclusion is further demonstrated by the results of electronic structure evolution for Ni atoms. As shown in Fig. 3e, the representative Ni atom, namely Ni12, shows a decreased valence state for both MD-Ni and MD-NiO due to its ability to accept electrons from Mg or Al atoms under an O-deficient atmosphere. In an O-rich atmosphere, the highly electronegative O atoms tend to accept electrons from Ni, Mg,

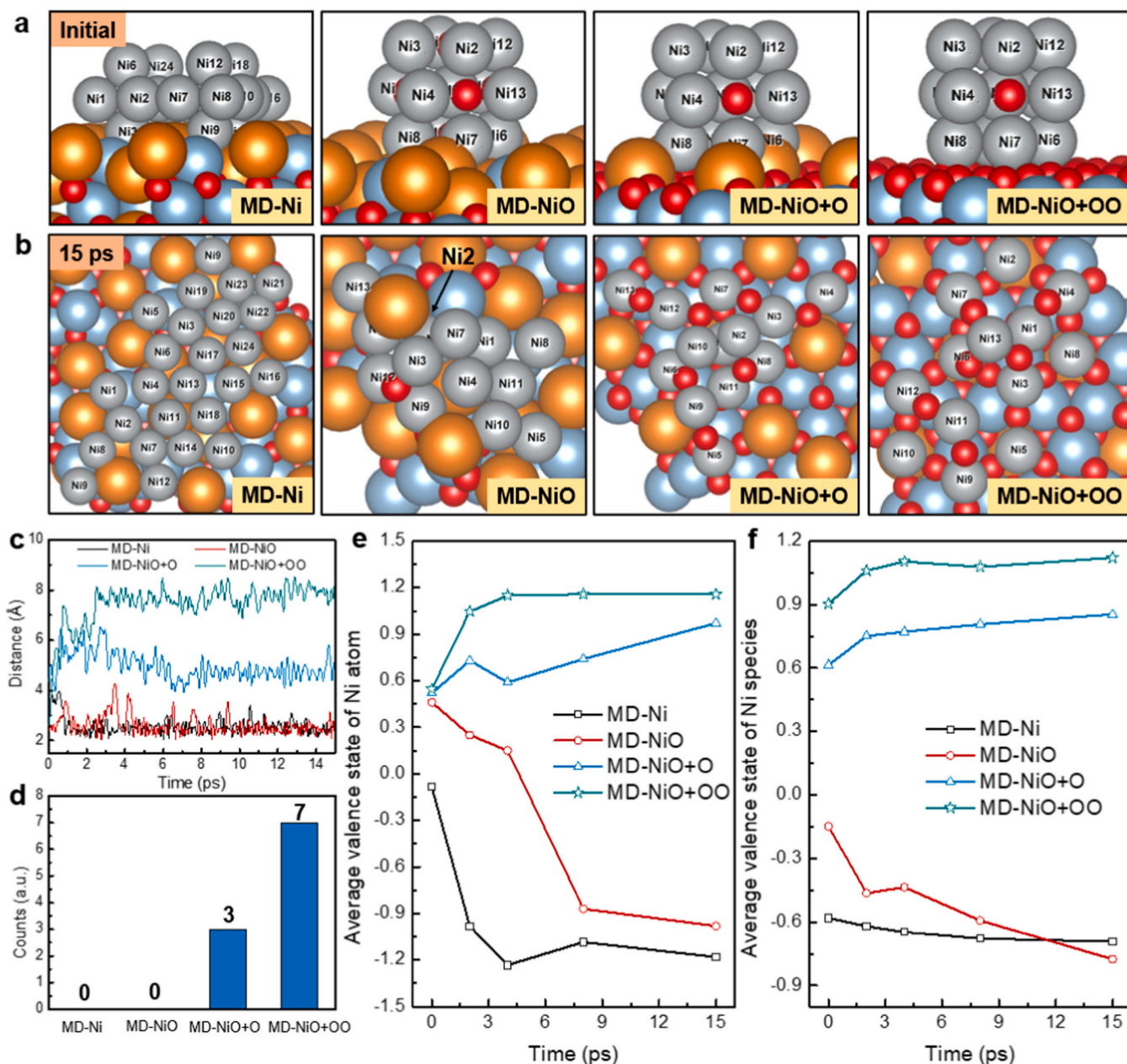


Fig. 3. (a) Front view of initial structure model and (b) top view of structure model after 15-ps MD calculations under given conditions for Ni or NiO on MgAl_2O_4 with different O coverage, atoms: Ni (gray), O (red), Al (blue), Mg (brown). (c) Number of redispersed Ni atoms after 15-ps MD calculations. (d) Evolution of distance between the typical Ni12 and Ni7 atoms for MD-Ni, and Ni12 and Ni2 atoms for MD-NiO, MD-NiO+O, and MD-NiO+OO. (e) Evolution of valence state for the Ni12 atom. (f) Evolution of average valence state for all Ni atoms.

and Al atoms to form Ni-O-Mg and Ni-O-Al bonding, which facilitates the migration of Ni atoms from NiO to MgAl_2O_4 . Furthermore, the average valence state of Ni species for the four models also exhibits a similar tendency to that of a single Ni atom, which further demonstrates the redispersion of Ni atoms promoted by O atoms (Fig. 3f). Notably, there appears to be an optimal amount of O atoms that can maintain the average valence state of Ni at a constant value and form a stable structure of Ni/ MgAl_2O_4 in such a redox atmosphere. This implies that the coverage of O-containing species in a redox-catalyzed process needs to remain constant, which is determined by the kinetic behavior of the catalyst for the specific catalytic reaction. However, it is well known that the kinetic behavior of the catalyst will inevitably change when the conversion of feedstock is high in a practical industrial catalytic process, leading to different structural damage depending on the structural sensitivity of the catalyst to a redox environment [28]. This also inspires

us that an ideal catalyst should have sufficient structural tolerance to the redox atmosphere against catalyst deactivation.

3.3. Spontaneous regeneration of active sites

Although the redispersion of Ni species inevitably leads to catalyst deactivation for Ni/ MgAl_2O_4 , it also facilitates the regeneration of deactivated catalysts due to sintering and coking by simply calcining the catalysts in an oxidizing atmosphere. In this work, a regeneration process for the deactivated Ni/ MgAl_2O_4 catalyst was also carried out, in which CO_2 , one of the feedstocks for DRM, is used as an oxidizer to redisperse Ni and remove coke [50]. As shown in Fig. S15, after the regeneration process, the conversions of CO_2 and CH_4 can return to their initial levels, and three regeneration cycles further confirm the cyclic stability of the Ni/ MgAl_2O_4 catalyst. Notably, the atmosphere near the

inlet during DRM reaction is oxidizing enough to achieve the redispersion of Ni species. The regeneration process indicates that the atmosphere near the outlet is highly reducing to cause the segregation of redispersed Ni species in MgAl_2O_4 . As the redispersion and the sintering of Ni species are reversible, i.e., the CO/H_2 atmosphere near the outlet might be able to regenerate the deactivated sites due to redispersion, the CO_2/CH_4 atmosphere near the inlet might be able to regenerate the deactivated sites due to sintering and coking. Therefore, spontaneous regeneration of the active sites to obtain good long-term stability without shutting down the reaction to replace or regenerate the spent catalysts could be simply achieved by periodically switching the flow direction of reaction gases. To demonstrate this concept, a pneumatic four-way valve is introduced to construct an alternating gas (AG) feeding mode.

feeding mode similar to an alternating current (Fig. 4a). Surprisingly, the $\text{Ni}/\text{MgAl}_2\text{O}_4$ catalyst shows continuous $\sim 90\%$ CO_2 and CH_4 conversions and a $\sim 95\%$ H_2/CO ratio without any deactivation during 50-h DRM reaction using this AG feeding strategy by switching the four-way valve once an hour, which directly indicates the success of this AG strategy against catalyst deactivation (Figs. 4b and S16). Moreover, unlike the spent catalyst bed using the conventional direct gas (DG) feeding mode, the spent catalysts bed using the AG feeding strategy shows a homogenous color distribution with a uniform Ni particle size of ~ 16.8 nm and no coke formation (Fig. 4c-e and S17). Meanwhile, both the Ni species near the inlet and outlet exhibit similar electronic structures close to metallic Ni, indicating that such an AG feeding strategy balances the distribution of redox atmosphere across the catalyst bed so

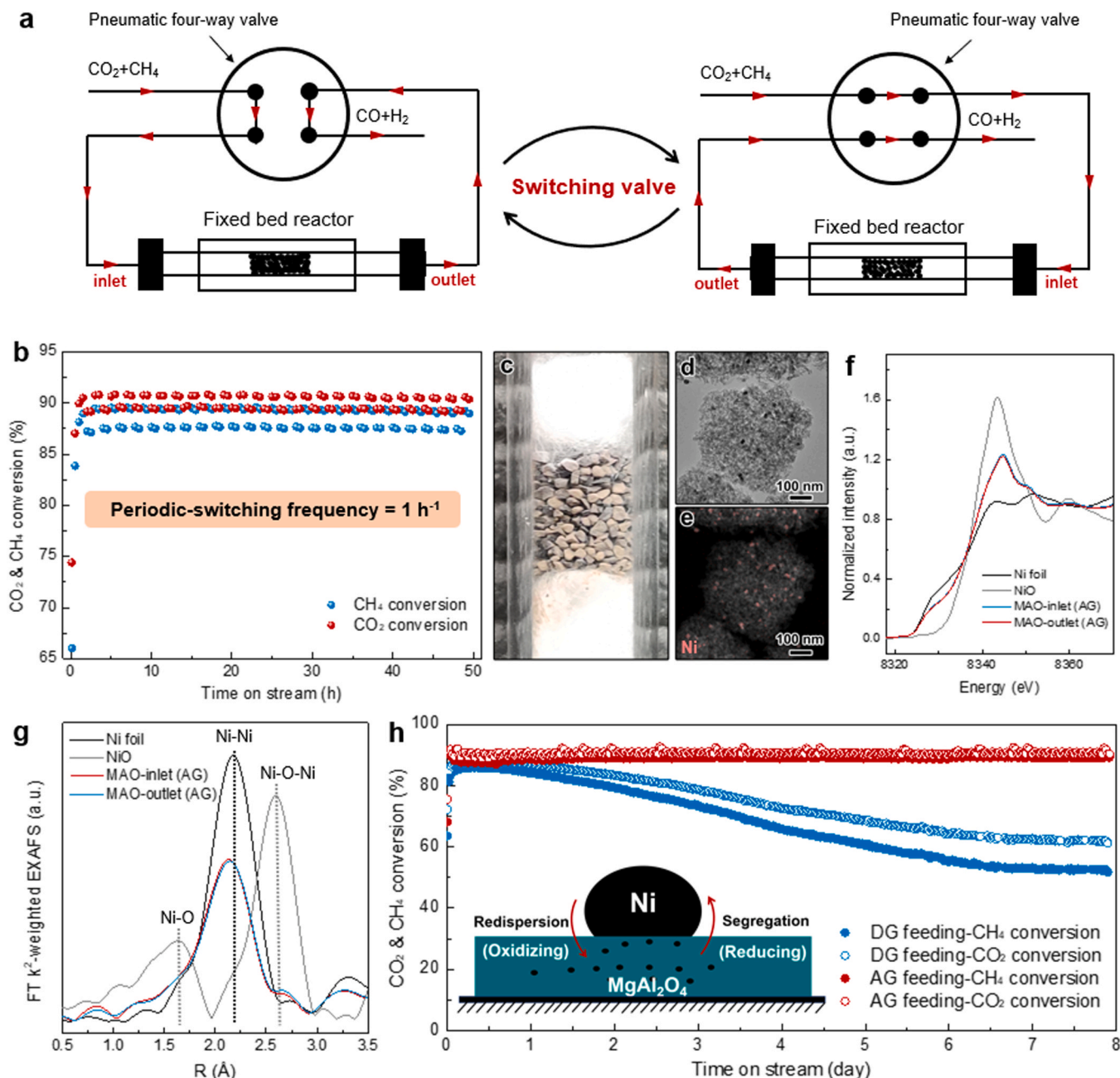


Fig. 4. (a) Schematic illustration of the AG feeding strategy. (b) Evolution of CH_4 and CO_2 conversions for $\text{Ni}/\text{MgAl}_2\text{O}_4$ during 50-h DRM catalytic reaction at 800°C using the AG feeding strategy (30 mg catalysts, 40–60 mesh, $\text{CO}_2/\text{CH}_4/\text{N}_2 = 20/20/40$ ml/min, periodic-switching frequency of pneumatic four-way valve is 1 h^{-1}). (c) Digital photo, (d) TEM image, and (e) EDX elemental mapping of $\text{Ni}/\text{MgAl}_2\text{O}_4$ after 50-h DRM catalytic reaction using the AG feeding strategy. (f) XANES and (g) EXAFS spectra for spent $\text{Ni}/\text{MgAl}_2\text{O}_4$ catalysts near the inlet and outlet of the catalyst bed. (h) Evolution of CH_4 and CO_2 conversions for $\text{Ni}/\text{MgAl}_2\text{O}_4$ during 8-day DRM catalytic reaction at 800°C using the AG and DG feeding strategies.

that the loss of active Ni sites due to redispersion, sintering and coking can be neglected (Figs. 4f, g, and S18). Such an AG feeding strategy results in a cyclic change in the number of active sites as the reaction proceeds, which first decreases due to sintering, redispersion of Ni nanoparticles, and coking, then gradually returns to the initial level through spontaneous regeneration induced by inlet-outlet switching operations. Repeating this cycle during a longer-term catalytic process will maintain the number of active sites in the catalyst within a relatively constant range thereby inhibiting catalyst deactivation. In other words, the AG feeding strategy creates a homogeneous local redox environment across the catalyst bed ensuring a stable catalyst structure based on its structural sensitivity. Furthermore, high feedstock conversion in DRM catalytic processes may also result in a non-uniform distribution of mass/heat transfer effects along the catalyst bed, which can be eliminated by employing our AG strategy. Longer-term stability tests for DRM over Ni/MgAl₂O₄ catalysts were also conducted to compare the two feeding strategies. The AG feeding strategy achieves supra-stable DRM reaction for 8 days, while the DG feeding strategy exhibits approximately a 30% decrease in conversions of CO₂ and CH₄ (Figs. 4h and S19). Furthermore, the spent catalysts using the AG feeding strategy were also successively subjected to oxidizing and reducing atmospheres, and the catalyst still shows the structure sensitivity to redox environments (Fig. S20). These results indicate that the AG feeding strategy could be a potential visible process for industrial-scale DRM reaction and an effective way for inhibiting catalyst deactivation in various redox catalytic processes. We believe that the current AG feeding strategy, as a modification of the fixed-bed reactor, can effectively address issues related to activity, selectivity, and stability caused by non-uniform distribution of the redox atmosphere in the catalyst bed. Furthermore, this study on the AG strategy also lays a theoretical foundation for future industrial-scale moving bed operation.

4. Conclusions

In summary, we demonstrated the reversible deactivation behaviors of Ni-MgAl₂O₄ catalysts with strong metal-support interaction, i.e., the loss of Ni active sites due to oxidation/redispersion in an oxidizing atmosphere and sintering in a reducing atmosphere. Therefore, we proposed a simple alternating gas (AG) feeding strategy to exploit the unique atmosphere-dependent structural evolution property of Ni-MgAl₂O₄ catalysts for achieving *in-situ* spontaneous regeneration of active sites against catalyst deactivation, enabling an ultra-stable DRM process. The fundamental understanding of the sensitivity of catalyst structure to the redox atmosphere during DRM reaction can also be generally applicable for various redox catalytic processes, which could inspire the optimization of catalyst design or catalytic engineering to enhance performance in many challenged high-temperature catalytic processes.

CRediT authorship contribution statement

Zhang Chengcheng: Investigation, Methodology. **Chen Yuxin:** Investigation, Methodology. **He Le:** Methodology, Supervision. **Xue Qiangqiang:** Investigation, Methodology. **Wang Yujun:** Methodology, Supervision. **Zhang Jiajun:** Conceptualization, Methodology, Software, Investigation, Funding acquisition. **Zhang Xiaohong:** Methodology, Supervision. **Feng Kai:** Investigation, Methodology, Visualization, Writing – original draft, Conceptualization, Funding acquisition. **Liu Xiaozhi:** Investigation, Methodology. **Su Dong:** Methodology, Supervision. **Li Zhengwen:** Investigation, Methodology. **Yang Bin:** Methodology, Supervision. **Yan Binhang:** Conceptualization, Funding acquisition, Writing – review & editing. **Wu Zhiyi:** Investigation, Methodology. **Luo Kai Hong:** Conceptualization, Funding acquisition, Supervision, Writing – review & editing. **Pan Yue:** Investigation, Methodology. **Tian Jiaming:** Investigation, Methodology, Software.

Declaration of Competing Interest

The authors declare that they have no known competing financial interests or personal relationships that could have appeared to influence the work reported in this paper.

Data availability

Data will be made available on request.

Acknowledgements

This work was supported by the National Natural Science Foundation of China (NSFC, Grant No. 21978148 and 52206156) and Project funded by China Postdoctoral Science Foundation (Grant No. 2021M691766, 2021M701851 and 2022T150349). The authors thank beamline 4B9A and 1W1B at the Beijing Synchrotron Radiation Facility (BSRF) and beamline BL14B1 at the Shanghai Synchrotron Radiation Facility (SSRF) for providing the beam time. Support from the UK Engineering and Physical Sciences Research Council under the project “UK Consortium on Mesoscale Engineering Sciences (UKCOMES)” (Grant No. EP/R029598/1 and EP/X035875/1) is gratefully acknowledged. This work made use of computational support by CoSeC, the Computational Science Centre for Research Communities, through UKCOMES.

Appendix A. Supporting information

Supplementary data associated with this article can be found in the online version at doi:10.1016/j.apcatb.2023.123647.

References

- [1] C.H. Bartholomew, Mechanisms of catalyst deactivation, *Appl. Catal. A* 212 (2001) 17–60.
- [2] G. Prieto, J. Zecevic, H. Friedrich, K.P. de Jong, P.E. de Jongh, Towards stable catalysts by controlling collective properties of supported metal nanoparticles, *Nat. Mater.* 12 (2013) 34–39.
- [3] A.J. Martín, S. Mitchell, C. Mondelli, S. Jaydev, J. Pérez-Ramírez, Unifying views on catalyst deactivation, *Nat. Catal.* 5 (2022) 854–866.
- [4] M. Argyle, C. Bartholomew, Heterogeneous catalyst deactivation and regeneration: a review, *Catalysts* 5 (2015) 145–269.
- [5] T.W. Hansen, A.T. Delariva, S.R. Challa, A.K. Datye, Sintering of catalytic nanoparticles: particle migration or Ostwald ripening? *Acc. Chem. Res.* 46 (2013) 1720–1730.
- [6] J. Jones, H. Xiong, A.T. DeLaRiva, E.J. Peterson, H. Pham, S.R. Challa, G. Qi, S. Oh, M.H. Wiebenga, X.I. Pereira Hernandez, Y. Wang, A.K. Datye, Thermally stable single-atom platinum-on-ceria catalysts via atom trapping, *Science* 353 (2016) 150–154.
- [7] X. Li, X.I. Pereira-Hernandez, Y. Chen, J. Xu, J. Zhao, C.W. Pao, C.Y. Fang, J. Zeng, Y. Wang, B.C. Gates, J. Liu, Functional CeOx nanoglues for robust atomically dispersed catalysts, *Nature* 611 (2022) 284–288.
- [8] Y. Wang, R. Zhang, B. Yan, Ni/CeO₂/9EuO_{1.01}95 with enhanced coke resistance for dry reforming of methane, *J. Catal.* 407 (2022) 77–89.
- [9] B. Zhao, B. Yan, S. Yao, Z. Xie, Q. Wu, R. Ran, D. Weng, C. Zhang, J.G. Chen, LaFeO₃/9NiO_{1.03} perovskite catalyst with enhanced activity and coke-resistance for dry reforming of ethane, *J. Catal.* 358 (2018) 168–178.
- [10] J. Lu, B. Fu, M.C. Kung, G. Xiao, J.W. Elam, H.H. Kung, P.C. Stair, Coking- and sintering-resistant palladium catalysts achieved through atomic layer deposition, *Science* 335 (2012) 1205–1208.
- [11] E.D. Goodman, A.C. Johnston-Peck, E.M. Dietze, C.J. Wrasman, A.S. Hoffman, F. Abild-Pedersen, S.R. Bare, P.N. Plessow, M. Cargnello, Supported catalyst deactivation by decomposition into single atoms is suppressed by increasing metal loading, *Nat. Catal.* 2 (2019) 748–755.
- [12] T. Margossian, K. Larmier, S.M. Kim, F. Krumeich, A. Fedorov, P. Chen, C. R. Muller, C. Coperet, Molecularly tailored nickel precursor and support yield a stable methane dry reforming catalyst with superior metal utilization, *J. Am. Chem. Soc.* 139 (2017) 6919–6927.
- [13] H. Li, C. Hao, J. Tian, S. Wang, C. Zhao, Ultra-durable Ni-Ir/MgAl₂O₄ catalysts for dry reforming of methane enabled by dynamic balance between carbon deposition and elimination, *Chem. Catal.* 2 (2022) 1748–1763.
- [14] G.W. Huber, S. Iborra, A. Corma, Synthesis of transportation fuels from biomass: chemistry, catalysts, and engineering, *Chem. Rev.* 106 (2006) 4044–4098.
- [15] R. Blom, I.M. Dahl, Å. Slagtem, B. Sortland, A. Spjelkavik, E. Tangstad, Carbon dioxide reforming of methane over lanthanum-modified catalysts in a fluidized-bed reactor, *Catal. Today* 21 (1994) 535–543.

- [16] E.T. Vogt, B.M. Weckhuysen, Fluid catalytic cracking: recent developments on the grand old lady of zeolite catalysis, *Chem. Soc. Rev.* 44 (2015) 7342–7370.
- [17] Z. Zhu, K. Feng, C. Li, R. Tang, M. Xiao, R. Song, D. Yang, B. Yan, L. He, Stabilization of exposed metal nanocrystals in high-temperature heterogeneous catalysis, *Adv. Mater.* 34 (2022), e2108727.
- [18] Y. Liu, Y. Chen, Z. Gao, X. Zhang, L. Zhang, M. Wang, B. Chen, Y. Diao, Y. Li, D. Xiao, X. Wang, D. Ma, C. Shi, Embedding high loading and uniform Ni nanoparticles into silicalite-1 zeolite for dry reforming of methane, *Appl. Catal.*, B 307 (2022), 121202.
- [19] S. Wang, K. Feng, D. Zhang, D. Yang, M. Xiao, C. Zhang, L. He, B. Yan, G.A. Ozin, W. Sun, Stable Cu catalysts supported by two-dimensional SiO₂ with strong metal-support interaction, *Adv. Sci.* 9 (2022), e2104972.
- [20] L. Wang, L. Wang, X. Meng, F.S. Xiao, New strategies for the preparation of sinter-resistant metal-nanoparticle-based catalysts, *Adv. Mater.* 31 (2019), e1901905.
- [21] S. Hu, W.X. Li, Sabatier principle of metal-support interaction for design of ultrastable metal nanocatalysts, *Science* 374 (2021) 1360–1365.
- [22] T.W. van Deelen, C. Hernández Mejía, K.P. de Jong, Control of metal-support interactions in heterogeneous catalysts to enhance activity and selectivity, *Nat. Catal.* 2 (2019) 955–970.
- [23] A. Aitbekova, L. Wu, C.J. Wrasman, A. Boubnov, A.S. Hoffman, E.D. Goodman, S. R. Bare, M. Cargnello, Low-temperature restructuring of CeO₂-supported Ru nanoparticles determines selectivity in CO₂ catalytic reduction, *J. Am. Chem. Soc.* 140 (2018) 13736–13745.
- [24] R. Li, X. Xu, B. Zhu, X.Y. Li, Y. Ning, R. Mu, P. Du, M. Li, H. Wang, J. Liang, Y. Chen, Y. Gao, B. Yang, Q. Fu, X. Bao, In situ identification of the metallic state of Ag nanoclusters in oxidative dispersion, *Nat. Commun.* 12 (2021) 1406.
- [25] R. Lang, W. Xi, J.C. Liu, Y.T. Cui, T. Li, A.F. Lee, F. Chen, Y. Chen, L. Li, L. Li, J. Lin, S. Miao, X. Liu, A.Q. Wang, X. Wang, J. Luo, B. Qiao, J. Li, T. Zhang, Non defect-stabilized thermally stable single-atom catalyst, *Nat. Commun.* 10 (2019), 234.
- [26] L. Lin, J. Liu, X. Liu, Z. Gao, N. Rui, S. Yao, F. Zhang, M. Wang, C. Liu, L. Han, F. Yang, S. Zhang, X.D. Wen, S.D. Senanayake, Y. Wu, X. Li, J.A. Rodriguez, D. Ma, Reversing sintering effect of Ni particles on gamma-Mo₂N via strong metal support interaction, *Nat. Commun.* 12 (2021) 6978.
- [27] C.Y. Liu, A.J. Bard, Pressure-induced insulator conductor transition in a photoconducting organic liquid-crystal film, *Nature* 418 (2002) 162–164.
- [28] I.S. Metcalfe, B. Ray, C. Dejoie, W. Hu, C. de Leeuwe, C. Dueso, F.R. Garcia-Garcia, C.M. Mak, E.I. Papaioannou, C.R. Thompson, J.S.O. Evans, Overcoming chemical equilibrium limitations using a thermodynamically reversible chemical reactor, *Nat. Chem.* 11 (2019) 638–643.
- [29] X. Zhang, Y. Xu, Y. Liu, L. Niu, Y. Diao, Z. Gao, B. Chen, J. Xie, M. Bi, M. Wang, D. Xiao, D. Ma, C. Shi, A novel Ni–MoC_xO_y interfacial catalyst for syngas production via the chemical looping dry reforming of methane, *Chem* 9 (2022) 1–15.
- [30] D. Pakhare, J. Spivey, A review of dry (CO₂) reforming of methane over noble metal catalysts, *Chem. Soc. Rev.* 43 (2014) 7813–7837.
- [31] C. Palmer, D.C. Upham, S. Smart, M.J. Gordon, H. Metiu, E.W. McFarland, Dry reforming of methane catalysed by molten metal alloys, *Nat. Catal.* 3 (2020) 83–89.
- [32] S. Shoji, X. Peng, A. Yamaguchi, R. Watanabe, C. Fukuhara, Y. Cho, T. Yamamoto, S. Matsumura, M.-W. Yu, S. Ishii, T. Fujita, H. Abe, M. Miyauchi, Photocatalytic uphill conversion of natural gas beyond the limitation of thermal reaction systems, *Nat. Catal.* 3 (2020) 148–153.
- [33] L. Zhou, J.M.P. Martinez, J. Finzel, C. Zhang, D.F. Swearer, S. Tian, H. Robatjazi, M. Lou, L. Dong, L. Henderson, P. Christopher, E.A. Carter, P. Nordlander, N. J. Halas, Light-driven methane dry reforming with single atomic site antenna-reactor plasmonic photocatalysts, *Nat. Energy* 5 (2020) 61–70.
- [34] Q. Xue, B. Yan, Y. Wang, G. Luo, Continuous synthesis of atomically dispersed Rh supported on MgAl₂O₄ using two-stage microreactor, *AlChE J.* 68 (2022), e17841.
- [35] J.P. Perdew, K. Burke, M. Ernzerhof, Generalized gradient approximation made simple, *Phys. Rev. Lett.* 77 (1996) 3865–3868.
- [36] S. Grimme, Semiempirical GGA-type density functional constructed with a long-range dispersion correction, *J. Comput. Chem.* 27 (2006) 1787–1799.
- [37] K. Lejaeghere, V. Van Speybroeck, G. Van Oost, S. Cottenier, Error estimates for solid-state density-functional theory predictions: an overview by means of the ground-state elemental crystals, *Crit. Rev. Solid State Mater. Sci.* 39 (2014) 1–24.
- [38] C.J. Pickard, B. Winkler, R.K. Chen, M.C. Payne, M.H. Lee, J.S. Lin, J.A. White, V. Milman, D. Vanderbilt, Structural properties of lanthanide and actinide compounds within the plane wave pseudopotential approach, *Phys. Rev. Lett.* 85 (2000) 5122–5125.
- [39] T. Yagi, H.K. Mao, P.M. Bell, Structure and crystal-chemistry of perovskite-type MgSiO₃, *Phys. Chem. Miner.* 3 (1978) 97–110.
- [40] L.C. Buelens, V.V. Galvita, H. Poelman, C. Detavernier, G.B. Marin, Super-dry reforming of methane intensifies CO₂ utilization via Le Chatelier's principle, *Science* 354 (2016) 449–452.
- [41] Q. Zhu, H. Zhou, L. Wang, L. Wang, C. Wang, H. Wang, W. Fang, M. He, Q. Wu, F.-S. Xiao, Enhanced CO₂ utilization in dry reforming of methane achieved through nickel-mediated hydrogen spillover in zeolite crystals, *Nat. Catal.* 5 (2022) 1030–1037.
- [42] K. Feng, J. Tian, M. Guo, Y. Wang, S. Wang, Z. Wu, J. Zhang, L. He, B. Yan, Experimentally unveiling the origin of tunable selectivity for CO₂ hydrogenation over Ni-based catalysts, *Appl. Catal. B* 292 (2021), 120191.
- [43] L. He, M. Li, W.-C. Li, W. Xu, Y. Wang, Y.-B. Wang, W. Shen, A.-H. Lu, Robust and coke-free Ni catalyst stabilized by 1–2 nm-thick multielement oxide for methane dry reforming, *ACS Catal.* 11 (2021) 12409–12416.
- [44] J. Guo, H. Lou, H. Zhao, D. Chai, X. Zheng, Dry reforming of methane over nickel catalysts supported on magnesium aluminate spinels, *Appl. Catal. A* 273 (2004) 75–82.
- [45] S.M. Kim, P.M. Abdala, T. Margossian, D. Hosseini, L. Foppa, A. Armutlulu, W. van Beek, A. Comas-Vives, C. Coperet, C. Muller, Cooperativity and dynamics increase the performance of NiFe dry reforming catalysts, *J. Am. Chem. Soc.* 139 (2017) 1937–1949.
- [46] M.M. Millet, G. Algara-Siller, S. Wrabetz, A. Mazheika, F. Girgsdies, D. Teschner, F. Seitz, A. Tarasov, S.V. Levchenko, R. Schlögl, E. Frei, Ni single atom catalysts for CO₂ activation, *J. Am. Chem. Soc.* 141 (2019) 2451–2461.
- [47] T. Margossian, K. Larmier, S.M. Kim, F. Krumeich, C. Müller, C. Copéret, Supported bimetallic NiFe nanoparticles through colloid synthesis for improved dry reforming performance, *ACS Catal.* 7 (2017) 6942–6948.
- [48] V. De Coster, N.V. Srinath, S.A. Theofanidis, L. Pirro, A. Van Alboom, H. Poelman, M.K. Sabbe, G.B. Marin, V.V. Galvita, Looking inside a Ni-Fe/MgAl₂O₄ catalyst for methane dry reforming via Mössbauer spectroscopy and in situ QXAS, *Appl. Catal. B* 300 (2022), 120720.
- [49] C.O. Augustin, K. Hema, L.J. Berchmans, R. Kalai Selvan, R. Saraswathi, Effect of Ce⁴⁺-substitution on the structural, electrical and dielectric properties of NiAl₂O₄ spinel, *Phys. Status Solidi (a)* 202 (2005) 1017–1024.
- [50] D. Wang, P. Littlewood, T.J. Marks, P.C. Stair, E. Weitz, Coking can enhance product yields in the dry reforming of methane, *ACS Catal.* (2022) 8352–8362.